

COVER PAGE

Document downloaded by @DAEL

Tue Nov 24 19:32:21 2026
For personal use

When automatic English translation is provided, only the original document is authentic.
The EAA cannot be held responsible of any translation error

Bibliographical reference

Influence of the Gap Flow of Axial Vehicle Cooling Fans on Radiated Narrowband and Broadband Noise, Marcus Becher, Roman Krusche, Matthias Tautz, Michael Mauß, Nils Springer, Florian Krömer and Stefan Becker, Acta Acustica **vol. 105** (Number 3), 2019, pp. 435-448

DOI
https://doi.org/10.3813/AAA.919326

Acta Acustica united with Acustica
Vol. 105 (2019) 435 – 448

DOI 10.3813/AAA.919326

Influence of the Gap Flow of Axial Vehicle Cooling Fans on Radiated Narrowband and Broadband Noise

Marcus Becher[1)], Roman Krusche[1)], Matthias Tautz[1)], Michael Mauß[2)], Nils Springer[2)], Florian Krömer[1)], Stefan Becker[1)]

[1)] Friedrich-Alexander University Erlangen-Nuremberg, Institute of Process Machinery and Systems Engineering, Cauerstr. 4, 91058 Erlangen, Germany. marcus.becher@man.eu

[2)] Brose Fahrzeugteile GmbH, Oldenburg, Gerhard-Stalling-Straße 62, 26135 Oldenburg, Germany

Summary

Numerical investigations on the sound radiation of low-speed axial vehicle cooling fans with different blade skew and gap geometries were carried out and validated by experiments. To reproduce similar installation conditions to those found in a vehicle, an overall system is considered which contains a radiator, the cooling fan and a combustion engine dummy. By modifying the gap geometry of a backward skewed fan, broadband noise between 150 Hz and 2500 Hz can be reduced measurably. To investigate both effects, the different broadband noise emission and the mechanisms which lead to the narrowband subharmonic peaks, a hybrid approach is chosen. Therefore a computational fluid dynamics (CFD) simulation is performed as a first step and the acoustics are computed afterwards. Initially, the sound radiation is calculated using an integral method described by Ffowcs-Williams and Hawkings (FWH) and is validated by measurements. Due to the limited possibility to locate the acoustic sources, a volume-based method is carried out. Thereby, the acoustic source terms are calculated based on the APE-2 formulation to separate acoustic from hydrodynamic effects in the acoustic near field. Afterwards the propagation of these acoustic sources are calculated and compared to measurement results as well. Using this approach, different gap flows and its mechanisms on sound production can be identified by correlating flow field with the acoustic field. The influence of the gap flow on tonal and broadband noise of the considered fan configurations is clarified.

PACS no. 43.20.-f, 43.28.-g

1. Introduction

The automotive industry and its suppliers are interested in the sound design of vehicles due to two reasons. On one hand, the acoustic impression is an important factor in the decision of a customer to purchase a particular vehicle. The second issue is the increasingly stringent legislation concerning vehicular emission in terms of rising noise pollution in major population centers.

In addition to the acoustical alignment and optimization of the overall vehicle, dominant noise sources, such as the axial cooling fan, are considered individually. To ensure the similar flow conditions existing in the vehicle a simplified overall system is investigated.

In axial fans, the mechanisms of noise generation are based on a multitude of flow phenomena. In addition to the tonal noise, which occurs due to periodical mechanisms, broadband noise is caused by stochastically distributed flow variables. Hereafter, the relevant mechanisms are described.

Received 8 May 2018,
accepted 5 March 2019.

Unsteady inflow conditions lead to the variation of the inflow velocity and angle of attack which causes pressure fluctuations on the fan blade surface. At an observers point located in the stationary reference system, a tonal frequency, known as blade passing frequency (BPF), is perceived due to the periodic passing of these fluctuating blade forces [1]. Inflow conditions with increased turbulence intensity, consisting of eddies with an integral length scale which is smaller than the chord length, leads to stochastically distributed pressure fluctuations at the leading edge that results in broadband noise [2, 3, 4]. The noise generated by the gap flow between the rotating ring and the housing is another mechanism whose sources highly contribute to the overall sound radiation. The gap flow is caused by the pressure gradient between the suction and the pressure side of the fan. Due to the pressure gradient, the air flows through the gap from the pressure side to the suction side and interacts with the inflow. The resulting structures impinge on the blades and cause tonal and broadband noise. Furthermore, eddy detachment at the trailing edge leads to transient loading at the surface of the blades. This mechanism produces tones as well [2].

© S. Hirzel Verlag · EAA

Document downloaded by @DAEL, 2026-11-24 19:32:23 - personal use only

The fluid mechanical and acoustic mechanisms of the gap flow have been investigated on single axial ring fans. Magne *et al.* [5] and Moreau *et al.* [6] use numerical simulations to investigate mechanisms linked to the gap flow which lead to subharmonic humps below the blade passing frequency. Zayani [3] carried out numerical simulations of different skewed axial fans to describe gap flow and to explain different efficiencies in experiments. Additionally, the impact of blade skew on the acoustical behaviour of axial cooling fans was investigated.

This work is focused on the calculation of acoustic sources and their propagation using a hybrid approach. Sound generation mechanisms, induced by the gap flow in axial cooling fan systems, are detected and associated to the subharmonic peaks and broadband noise in the measurements. The basis for this is formed by modifying gap geometry and skewness which results in different characteristics of the gap flow and sound radiation caused by this mechanism.

The numerical methods of aeroacoustics used in this paper are discussed in Section 2. The experimental and simulation setup are presented in Secion 3. In Section 4, measurement results are illustrated and discussed. The influence of gap geometry and fan blade skew on the flow field is analysed in Secion 5 based on CFD simulations. Subsequently, the impact of the resulting gap flow on the acoustic source mechanisms is investigated in Section 6.

2. Numerical methods for computational aeroacoustics

Regarding acoustic computations two methods are used. On one hand sound radiation towards a point of interest is calculated using the FWH integral method [7], which has been applied successfully for sound prediction at far-field points in the past. On the other hand, acoustic sources are calculated using the Perturbed Convective Wave Equation (PCWE) [8, 9] which is an extension of the APE-2 system by Ewert and Schröder [10]. The propagation of these sources is simulated in a next step using an FE-formulation [11].

2.1. Ffowcs-Williams and Hawkings method

The code used for the prediction of sound in this paper is called SPySI (sound prediction by surface integration) which is based on the Ffowcs- Williams and Hawkings method [12] and was developed at the Institute of Process Machinery and Systems Engineering, University of Erlangen-Nuremberg.

In order to localize the source terms and separate the sound components in the far-field spectrum, the integration surface on which the source terms are calculated varies. There is the porous integration surface which contains the relevant sound sources and is placed in the stationary domain between fan and radiator. Furthermore, sound sources which occur at the blade surfaces are used to calculate the sound pressure at the microphone position.

The generally known FWH equation can be simplified under the assumption of small Mach numbers, Ma < 0.3 (volume integration term can be neglected). This results in the following equation for the sound pressure $\tilde{p}$ at a microphone position base on an integration area positioned in the stationary domain described by y_i.

$$\tilde{p} = \frac{1}{4\pi c_0^2}\frac{\partial}{\partial t}\int_S \left[\frac{Q\cdot c + L_j r_j^n}{c\cdot r\left|M_r-1\right|}\right]_{\tau_e} \mathrm{d}S(y_j) - \frac{1}{4\pi c_0^2}\int_S \left[\frac{L_j r_j^n}{r^2\left|M_r-1\right|}\right]_{\tau_e} \mathrm{d}S(yj). \quad (1)$$

The source terms are

$$Q = \rho u_i n_i \quad (2)$$

$$L_j = \left(\rho u_i u_j + P_{ij}\right) n_i. \quad (3)$$

Herein c_0 denotes the ambient speed of sound, whereas M_r is referred to as the radial Mach number. r being the distance from a source to the observer. $u_i(x_k, t)$ describes the velocity field and n_i defines the normal vector on the integration surface. The compressible stress tensor reads $P_{ij} = (p - p_0)\delta_{ij} + \tau_{ij}$. With p_0 as ambient pressure, δ_{ij} as Kronecker delta and τ_{ij} as molecular stress tensor.

For a rotating integration surface described by a co-rotating coordinate system η_j, the following equation is used to calculate the sound pressure at a far-field microphone position:

$$\tilde{p} = \frac{1}{4\pi c_0^2}\frac{\partial}{\partial t}\int_S \left[\frac{Q\cdot c + L_j r_j^n}{c\cdot r\left|M_r-1\right|}\right]_{\tau_e} \mathrm{d}S(\eta_j) - \frac{1}{4\pi c_0^2}\int_S \left[\frac{L_j r_j^n}{r^2\left|M_r-1\right|}\right]_{\tau_e} \mathrm{d}S(\eta_j). \quad (4)$$

With the source terms calculated in a rotating system:

$$Q = \left((\rho u_i - v_i) + \rho_0 v_i\right) n_i, \quad (5)$$

$$L_j = \left(\rho u_j (u_i - v_i) + P_{ij}\right) n_i. \quad (6)$$

Therein v_i indicates the velocity of a moving surface. For the calculation an advanced time algorithm [13] is implemented in SPySI.

2.2. Perturbed Convective Wave Equation

Apart from Lighthill's frequently used approach [14, 15], the calculation of acoustic source terms and their propagation in an acoustic domain is possible via the Acoustic Perturbation Equations (APE), which are implemented in the inhouse code `CFS++` [11]. By splitting the field variables velocity u_i, pressure p and density ρ into temporal mean $(\overline{\cdots})$, incompressible flow (superscript ^{ic}) and compressible acoustic (superscript ^{a}) components

$$\begin{aligned} u_i &= \overline{u}_i + u_i^{ic} + u_i^a, \\ p &= \overline{p} + p^{ic} + p^a, \\ \rho &= \overline{\rho} + \rho^{ic} + \rho^a, \end{aligned} \quad (7)$$

Document downloaded by @DAEL, 2026-11-24 19:32:23 - personal use only

and introducing them into the mass and momentum conservation equations, one arrives at a set of partial differential equations, referred to as APE-2 system [8, 10]. Additionally, constant ambient density ρ_0 and speed of sound c_0 are assumed throughout the whole domain as well as a low Mach number (Ma < 0.3) and an isothermal flow. Although solving the APE-2 system is possible, a scaler-valued wave equation is preferred due to the computational effort. This leads to the derivation of the Perturbed Convective Wave Equation (PCWE) by Hüppe *et al.* [8, 9],

$$\frac{1}{c_0^2}\frac{\mathrm{D}^2\phi^a}{\mathrm{D}t^2} - \frac{\partial^2\phi^a}{\partial x_i \partial x_i} = -\frac{1}{\rho_0 c_0^2}\frac{\mathrm{D}p^{ic}}{\mathrm{D}t}, \tag{8}$$

wherein ϕ^a denotes the scalar acoustic potential which is related to the acoustic particle velocity as

$$u_j^a = -\frac{\partial\phi^a}{\partial x_j}. \tag{9}$$

As can be seen in equation (8), the aeroacoustic source term is evaluated by the substantial derivative of the hydrodynamic pressure p^{ic} which is obtained by performing an incompressible CFD analysis. This convective wave equation is well suited for applications containing a rotating system. An FE formulation of the wave equation in rotating systems is also discussed in [8]. After solving the PCWE for the propagation domain the acoustic pressure

$$p^a = \rho_0\left(\frac{\partial\phi^a}{\partial t} + \bar{u}_i\frac{\partial\phi^a}{\partial x_i}\right) = \rho_0\frac{\mathrm{D}\phi^a}{\mathrm{D}t} \tag{10}$$

can be calculated in a post processing step.

3. Experimental and numerical setup

3.1. Experimental setup

Measurements are carried in a standardized inlet test chamber, based on ISO 5801:2007 [16]. The test chamber is built as an anechoic room, with absorbing walls and ceiling. In measurements the overall system is considered to reproduce the setup existing in a vehicle and includes a radiator, the axial cooling fan and a combustion engine dummy. The fan is driven by an external motor to avoid spurious sound radiation into the anechoic room. Hence, struts are not needed to stabilize any motor in the hub and are not considered in the following investigations. A schematic sectional view of the experimental setup is illustrated in Figure 1.

To investigate the influence of tip clearance recirculation on the flow field and sound radiation, a backward skewed axial fan with a standard gap geometry (BS) and a backward skewed fan with a modified gap geometry (BM) is taken into account. The blade skew has a significant influence on gap flow as well. Therefore, an additional fan with forward skewed blades and standard gap geometry (FS) is investigated. The backward skewed fans share the same blade geometry. For the forward skewed fan the sweep of the backward skewed fan is used in the forward

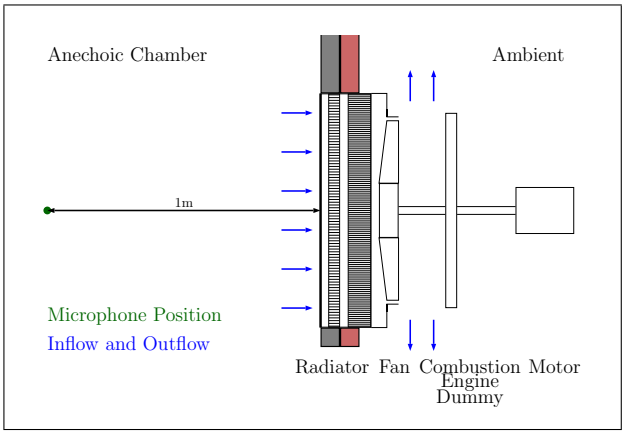


Figure 1. Schematic sectional view of the experimental setup.

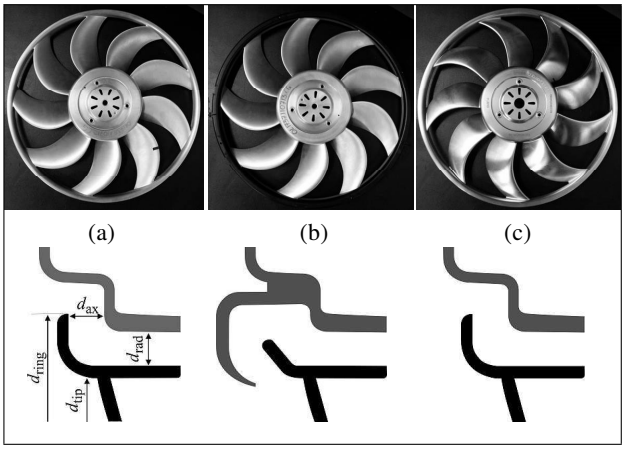


Figure 2. Counter-clockwise rotating cooling fans with varied blade skew and gap geometry. (a) BS, (b) BM, (c) FS.

direction. The backward skewed fans are designed for industrial application and can be found in modern cars. The forward skewed fan is just used for test applications. These three configurations (Figure 2) make it possible to influence the gap flow in a way to identify the mechanisms of sound production.

The nine-blade cooling fans have a tip diameter $d_{\mathrm{tip}} = 466\,\mathrm{mm}$ and a total diameter, also containing the ring which connects the blades $d_{\mathrm{ring}} = 492\,\mathrm{mm}$ for the standard gap geometry and $d_{ring} = 488\,\mathrm{mm}$ in the case of the modified gap configuration. The axial clearance d_{ax} between the ring and the housing is 7 mm in axial and 6 mm in radial direction (d_{rad}).

Inflow conditions have a high impact on the radiated sound by axial cooling fans. The turbulence intensity, downstream of the vehicle radiator, is usually distributed inhomogeneously due to its structure which includes several cooling packages. To avoid the influence of inhomogeneous turbulent inflow on the gap flow a simplified radiator model is designed which has a round shape and consists of two honeycomb flow straighteners (1). The channel diameter of the upstream honeycomb is 5 mm and in case of the of the downstream honeycomb it is 2 mm. The flow straighteners ensure a homogeneous flow field with a

Document downloaded by @DAEL, 2026-11-24 19:32:23 - personal use only

low turbulence intensity upstream of the fan. The pressure drop of the simplified radiator can be regulated using two perforated plates which can be moved against each other. The acoustic transmission of this radiator is comparable to that of vehicle radiators.

The outflow of axial cooling fans in vehicles is influenced by the combustion engine. To simplify the complex engine shape, a plate with a diameter of 460 mm is used and positioned 150 mm downstream of the radiator model. Consequently, the distance between the flow straighteners and the fans as well as the plate are kept constant for all investigated variants.

3.2. Numerical setup of the flow field

In Figure 3a a sectional view of the flow region of the CFD simulation is illustrated. To ensure comparability the structure for the computational domain is similar to the experimental setup. Thus, the computational domain consists of the cooler (c), the fan (f) and the combustion engine dummy (d). To make allowance for the rotation of the fan the numerical domain is separated into three sections, namely stationary inlet (I) and outlet (O) as well as a rotating domain (F). In the interest of the hybrid approach towards aeroacoustic analysis the in- and outlet domain for the flow simulation is kept small so that the computational time for the CFD is reduced. This can be done, since no recirculation areas close to in- and outlet surfaces are to be expected. This is due to the imposed mean flow direction along the fan axis at the inlet and the flow being perpendicular to the axis at the outlet respectively. The dimensions of the outlet domain were chosen based on former simulation results and velocity measurements using LDA.

Regarding boundary conditions, a free-field pressure setup of 0 Pa is specified at the in- and outlet surfaces. A rotational speed of 2400 rpm for the fan as well as no-slip wall conditions are assigned to the fan, the combustion engine dummy and the gap geometry. Artificial surfaces that are used to set the computational domain and which are not existent in the measurements are provided with slip wall conditions. The cooler is modelled using a porous media. To define the flow resistance of the cooler, measurements of pressure loss dependent on volumetric flow are used. The resulting characteristic curve is described by a function which consists of a linear and a quadratic term and its coefficients. These are used to implement the characteristics of the cooler in terms of flow resistance in the simulation software.

In terms of turbulence modeling the SAS-model (Scale Adaptive Simulation), an extended URANS-model first proposed by Menter [17], is applied for compressible and incompressible unsteady simulations. Therefore, a central difference spatial scheme as well as a second order backward Euler temporal scheme are used. In contrast to an URANS-model, the SAS model adapts turbulent structures in the flow field and consequently takes account for vortex decay. This ensures that smaller turbulent scales, which cause sound radiation in the middle and high frequency range are modeled more precisely. Nevertheless,

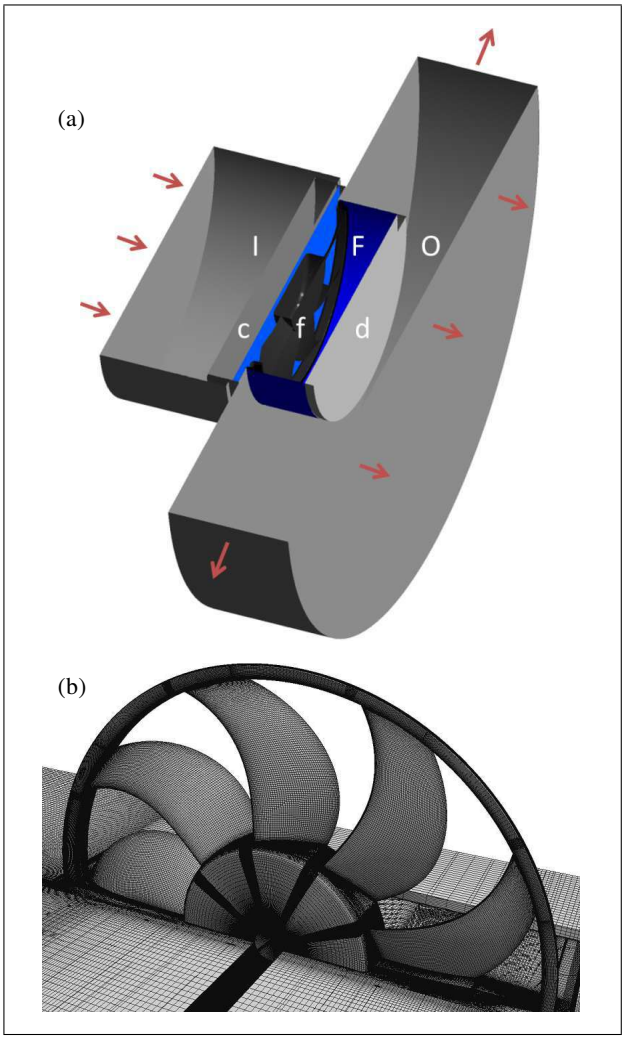


Figure 3. Computational domain for the CFD analysis. (a) Sectional view, (b) Mesh in rotating domain.

using the SAS turbulence model, a classical URANS is applied in steady flow regions which decreases the computational cost. In consequence, the grid resolution needs to be fine in turbulent regions or regions with a significant gradient in the flow variables, but can be relatively coarse in the steady flow regions. had to be calculated twice. On one hand the FWH approach requires compressible flow results, on the other hand incompressible flow results are necessary using the Perturbed Convective Wave Equation.

It is emphasized that due to the opposing acoustic approaches, namely the FWH method as well as the volume-based method, the flow field had to be calculated twice. In case of FWH method the acoustic sources are calculated based on the fluctuations of the flow variables at the integration surface. Hence, these fluctuations must be transported to the integrations surface which is achieved by a compressible flow simulation. In comparison, when computing the acoustic sources for the right hand side of the PCWE formulation an incompressible flow field is required.

Figure 3 illustrates the CFD-mesh for one of the simulated fan configurations, whereas the mesh only differs in

Document downloaded by @DAEL, 2026-11-24 19:32:23 - personal use only

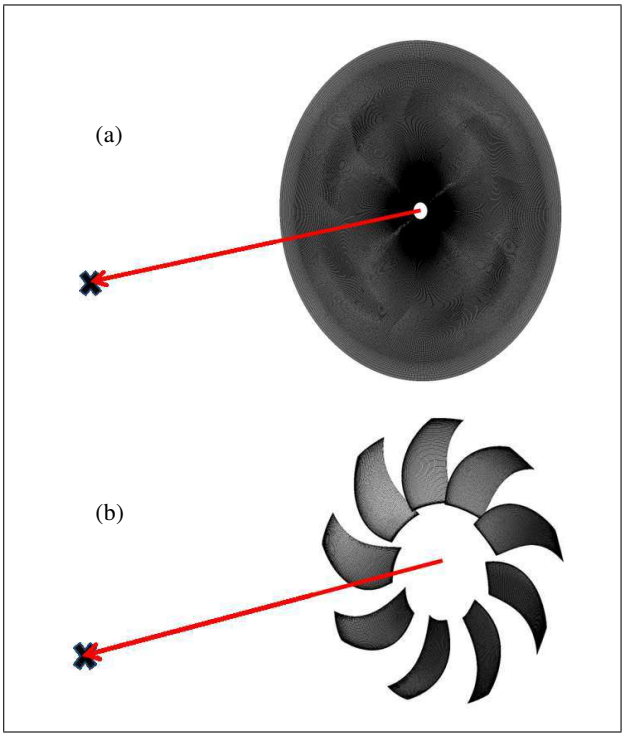


Figure 4. Different setups of the integration surface for the FWH calculations. (a) Stationary integration surface, (b) Integration surface in the rotating domain. X: Microphone positions.

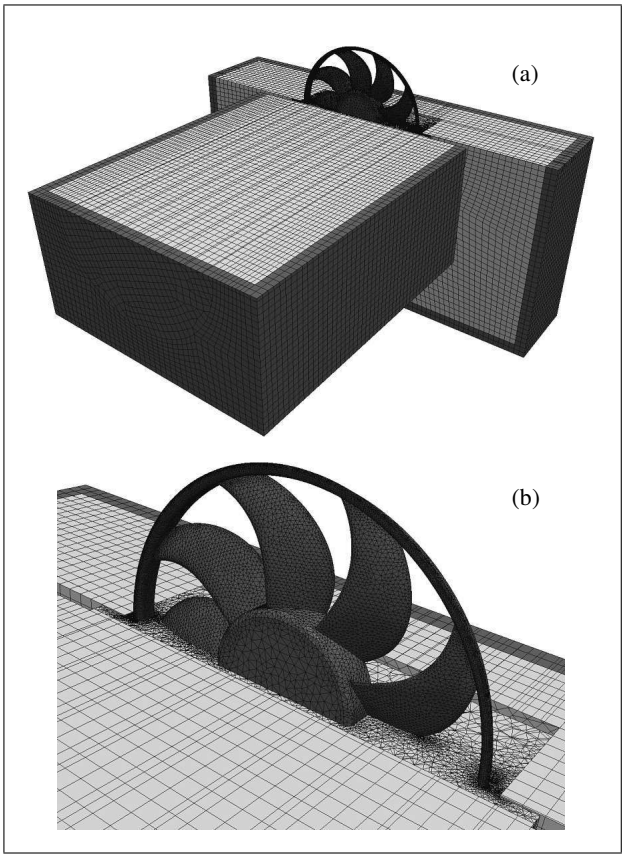


Figure 5. Mesh of the volume-based propagation simulation. (a) Mesh for acoustic domain surrounded by PML region on free field boundaries, (b) Mesh for rotating domain.

the rotational domain. For all three simulated configurations the number of grid nodes is about 64e6 including in- and outlet domain. The majority of nodes are located in the rotating region, particularly in the boundary layer around the fan blades and the tip clearance. A value of $y^+ \leq 1$ is achieved at the fan geometry as well as the housing. For the simulations carried out a time step $\Delta t = 7e-6\,\mathrm{s}$ is applied.

3.3. Numerical setup of the acoustic field

3.3.1. Integral method

In order to use SPySI for the FWH calculation, the flow variables of interest – the velocity components, the pressure and the density – are gathered from the permeable integration surface placed around the acoustic sources caused by the impeller. In these investigations, the integration surface is placed between the radiator and the fan in the stationary domain. It should be positioned as close as possible to the acoustic sources to avoid the influence of numerical damping to the acoustic results. The perfusion of the integration surface should not be turbulent or inhomogeneous at the same time. In case of the integration surface being positioned in the rotating domain, sound pressure is calculated based on flow variables on the blade surfaces. In this paper both approaches are investigated. The integration surfaces are illustrated in Figure 4.

From the integration surface Green's function given in [13] is used to calculate the acoustically relevant parameters at a point that corresponds to the microphone position in experiments. which is installed 1 m upstream of the radiator on the rotational axis. Owing to the use of Green's far-field function to derive the described equations (1) and (4), the existing radiator structure is not considered in FWH acoustic simulation.

3.3.2. Volume based method

Apart from the FWH approach the propagation of acoustic perturbations is computed by the FE solver `CFS++` [11]. In this case the PCWE, as discussed in Section 2, is solved on an additional mesh. The setup for the acoustic propagation calculation is analogous to the flow simulation (Figure 5). The inlet domain, however, is extended to include the microphone position on the axis 1 m upstream from the radiator.

To ensure acoustic free-field conditions on the boundary of the propagation region, a perfectly matched layer (PML) technique [18, 19] is applied on all surfaces of in- and outlet. With this technique the propagating waves are damped without reflecting back into the computational domain.

For calculating the acoustics in a hybrid approach the acoustic source terms are computed on a very fine CFD-mesh. For the acoustic propagation simulation, a coarser mesh than the CFD-mesh can be chosen in most of the domain. As a reference a resolution of 10 to 20 grid points per wavelength can be found in [20]. The number

Document downloaded by @DAEL, 2026-11-24 19:32:23 - personal use only

of grid points for the simulation is about 0.7e6 for all three fan configurations. For the acoustic simulation the source terms have to be conservatively interpolated to the coarse grid as described in [20]. The influence of the radiator structure is neglected in volume-based acoustic simulation as well.

4. Measurement Results

4.1. Characteristic curves

Figure 6 shows the fan characteristic curves of the three fan configurations. For the characteristic curve measurements, the fans were tested under free inflow conditions. In addition to the fan, the combustion engine dummy was part of the measurement. The total-to-static pressure coefficient ψ_{ts} is plotted dependent on the flow rate coefficient Φ which are defined as

$$\psi_{ts} = \frac{2\Delta p_{ts}}{\rho\left(D\pi n\right)^2}, \tag{11}$$

$$\Phi = \frac{4\dot{V}}{\pi^2 D^3 n}. \tag{12}$$

Compared to the backward skewed fan using the standard gap geometry, the pressure coefficient curve of BM shows slightly higher values from a flow rate coefficient higher than 0.1. Below 0.1, a stronger stall occurs in BM , resulting in lower pressure coefficient values. The characteristic of the forward skewed fan is different. On one hand, it shows the typical larger stall-free operational range below a flow rate coefficient of 0.1 and on the other hand the resulting pressure coefficient at higher flow rate coefficients is lower compared to the backward skewed fans. A reason for that is seen in the stronger axial velocity component forward skewed fans produce at the pressure side at the tip region [21, 22] which leads to a higher interaction of the flow with the combustion engine dummy. contribution of the velocity component in the axial direction to the absolute velocity This behaviour can be reproduced using stationary simulations.

In this paper the overall system including fan, combustion engine dummy and cooler is considered. Those systems are typically investigated at ambient pressure conditions in front of the radiator and after the combustion engine dummy. Using these conditions the flow rate coefficient is 0.115 for BM, 0.11 for BS and 0.096 for FS. Compared to the intersection points of the fan characteristic curve measured under free inflow conditions and the resistance curve of the cooler, the operating points are shifted towards smaller flow rate coefficients. This shows that the cooler has a significant influence on the inflow conditions of the fans which leads to lower pressure coefficients at the operating points. Furthermore, the pressure coefficients of these operation points do not match with the cooler resistance curve. The reason for this is additional pressure losses which occur in the overall system.

The differences of flow rate coefficient of the fans have to be taken into account when interpreting the results.

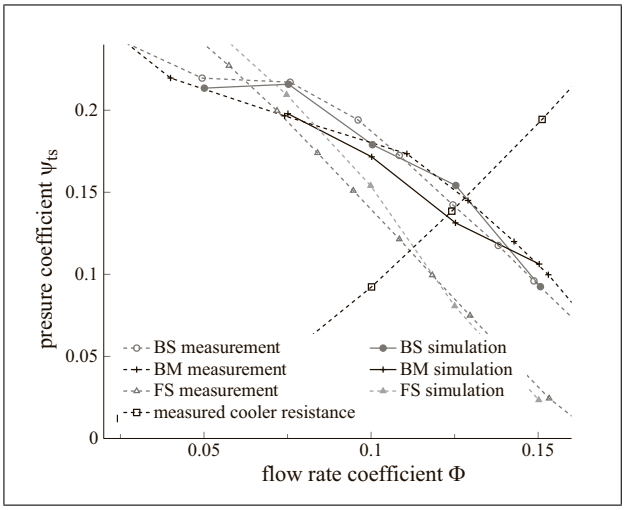


Figure 6. Measured and simulated fan characteristic curves and measured cooler resistance.

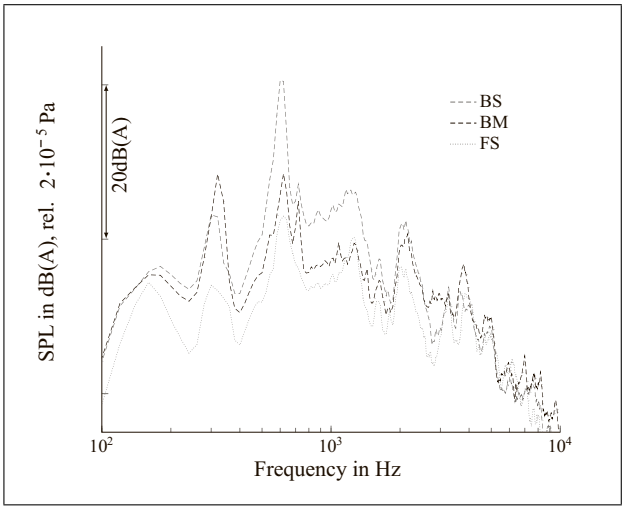


Figure 7. Measured spectra of sound pressure level (SPL) at a microphone position 1 m coaxial upstream of the radiator.

When considering the next section, it is noticeable that the fan BM shows lower sound emission than the variant BS from 150 Hz up to 2500 Hz.

4.2. Sound pressure spectra

Subsequently the acoustic measurement results are discussed. Therefore, the experimental setup as described in Section 3.1 is used.

On comparing the individual fan variants with each other, it can be determined that BS shows higher sound pressure levels from 150 Hz up to 2500 Hz than the other variants considering broadband noise. Regarding narrowband noise the subharmonic peaks at 300 Hz and its higher harmonics, particularly at 600 Hz dominate the spectra. The blade passing frequency is caused by spatially changing inflow conditions [3, 4]. These mechanisms are suppressed by the homogeneous inflow conditions of low turbulence intensity which occurs downstream of the radiator.

Document downloaded by @DAEL, 2026-11-24 19:32:23 - personal use only

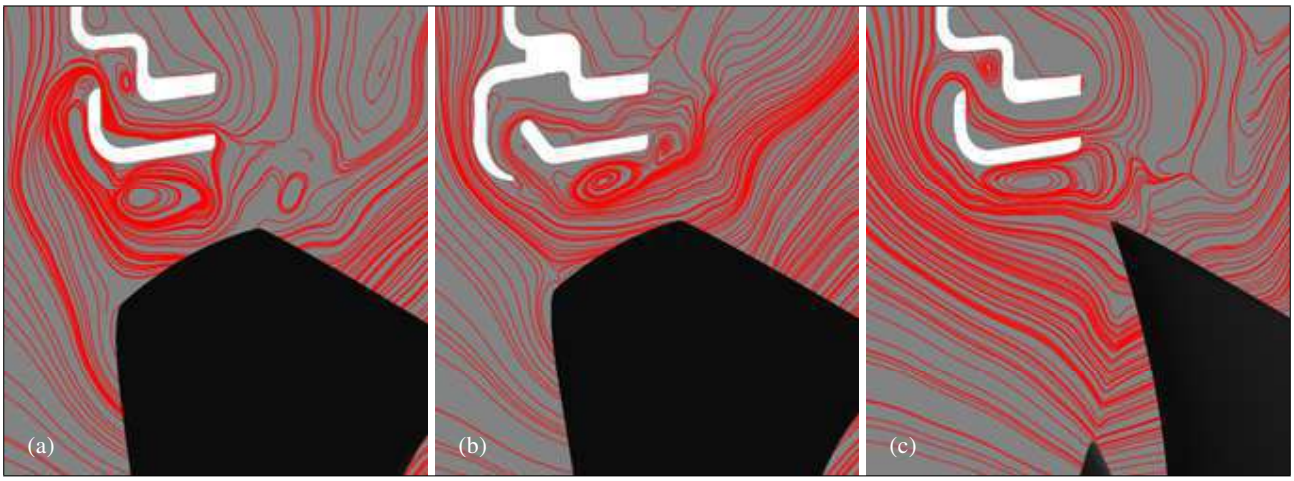


Figure 8. Recirculation area depending on housing and blade geometry. The location of the plane is illustrated in Figure 10.

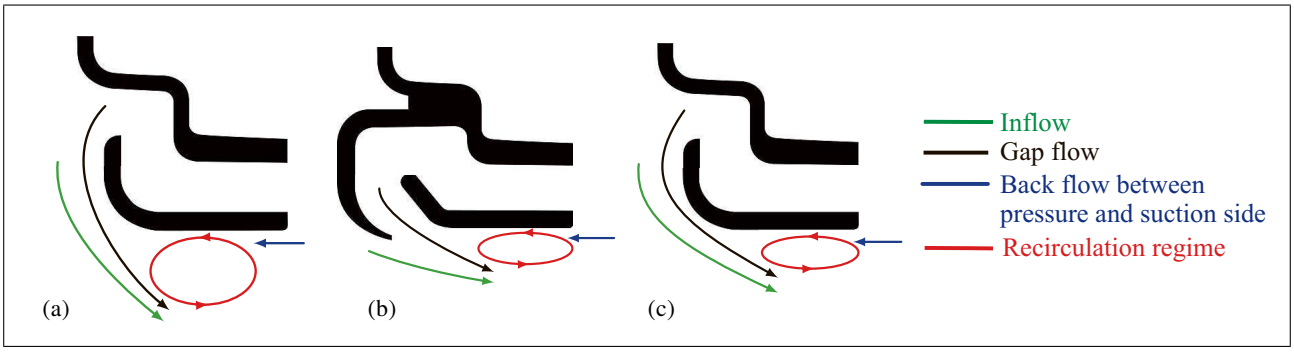


Figure 9. Mechanisms dependent on gap flow.

These two effects - different broadband and narrowband noise, dependent on fan and housing geometry - are investigated in the following sections.

5. Influence of gap geometry and blade skew on the gap flow

The influence of the gap and blade geometry on the gap flow is illustrated in Figure 8, which shows a sectional plane through the fan configurations with streamlines indicating the corresponding flow field.

In case of the standard gap geometry, the gap flow can exit the gap freely to the suction side of the fan and then interacts with the tip region of the blades differently. Considering BS the gap flow is deflected radially in the direction of the hub, whereas for the FS the axial component is more prominent. This is supported by the shape of the blade and the associated pressure field. For forward skewed fans, the profile sections are shifted away with decreasing radius considering a point at the blade tip. When the flow exits the gap between two blades it flows to the suction side of the blade tip where the lowest pressure occurs. Considering backward skewed fans, profile sections are shifted upstream with decreasing radius. When moving with the gap flow the closest, lowest pressure occurs for a profile section with a smaller radius in contrast to the forward skewed blades. Consequently, the gap flow is deflected towards the hub. The backflow directly beneath the ring occures mainly due to the pressure difference between discharge side and suction side. The interaction of the gap flow with the backflow results in the formation of a recirculation area beneath the ring.

In contrast to the axial flow at the tip region in front of the blade in case BM and FS, the radial flow component in the BS case supports the development of a large scale recirculation area below the ring. Of course, the pressure difference between the discharge side and suction side affects the backflow but the size of the recirculation area is mainly dictated by the direction of the inflow and gapflow in the tip region. As detected in the characteristic curves, the fan configuration BM shows the highest pressure difference. This does not lead to the formation of the largest recirculation area among the considered fan configurations. The effects which lead to the formation of the recirculation area are summarized in Figure 9.

The recirculation area impinges on the leading edge of the fan blades. Considering the remaining fans, the interaction can be reduced due to the convective transport of the turbulent structures in axial direction in case of BM and FS. In Figure 8 the discussed mean flow field is indicated by streamlines. The simulation shows that the gap flow is followed by a multitude of turbulent structures with different scales. Figure 10 illustrates iso-surfaces of veloc-

Document downloaded by @DAEL, 2026-11-24 19:32:23 - personal use only

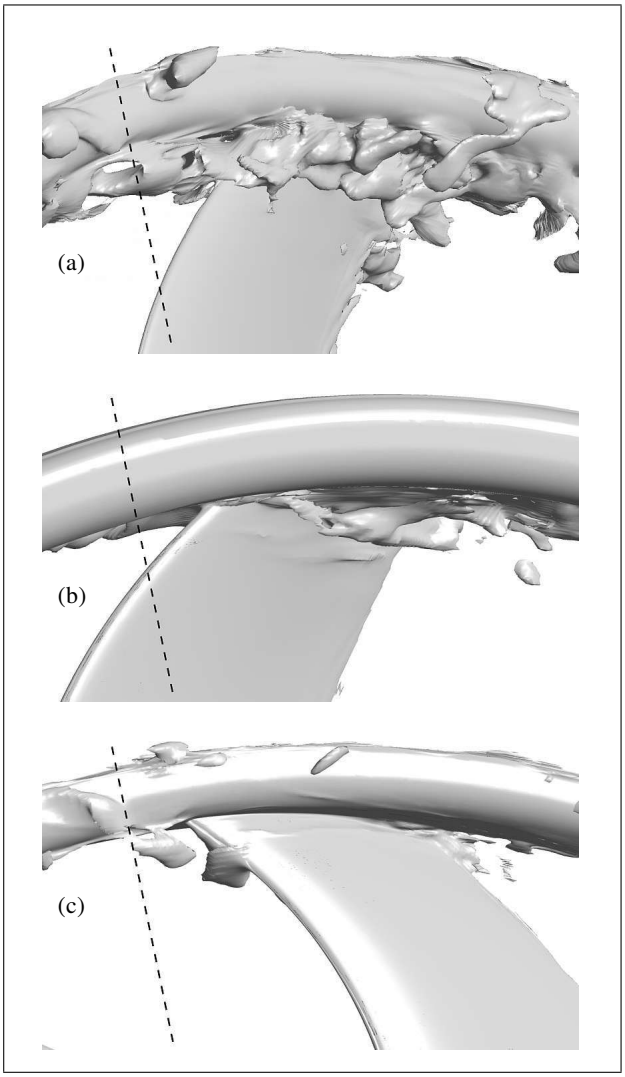


Figure 10. Iso-surfaces of velocity around blade tip. The dashed lines illustrate the location of the planes in Figures 8 and 21–23. (a) BS, (b) BM, (c) FS.

ity around the blade tips. According to the investigations of Magne *et al.* [5], Moreau *et al.* [6] and Zhu *et al.* [23], structures, moving with a reduced velocity compared to rotational speed of the fan, are responsible for narrowband sound at the subharmonic peaks when they impinge onto the leading edge.

The correlation of before mentioned structures with acoustic source terms will be pointed out in the following section. separations at the ring, the turbulent gap flow and by the interaction of gap flow and inflow. For the resulting turbulent flow field in the area of the gap and the blade tips, Figure 11 depicts the resulting pressure fluctuations on the blade surfaces.

The RMS value of these fluctuations shows that the largest area with increased pressure fluctuations is created in case of the configuration BS , due to the interaction between the blade and the turbulent structures. Analyzing the modified gap configuration, this area is clearly confined to the tip region. The forward skewed fan FS shows the strongest pressure fluctuations only in the vicinity of the leading edge.

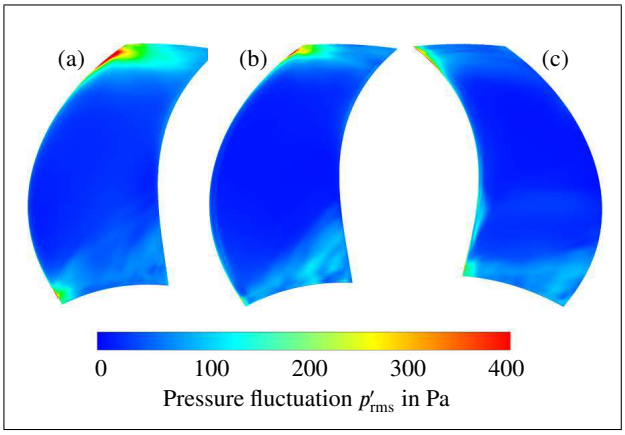


Figure 11. RMS value of pressure fluctuation on the fan blades. (a) BS, (b) BM, (c) FS.

6. Influence of gap flow on acoustical source mechanisms

6.1. Validation of calculated sound pressure spectra

In Figure 12 the calculated SPL using FWH method and the measured SPL on the axis 1 m upstream of the radiator are plotted. The source terms are calculated on an integration surface which is located in the stationary domain. The SPL is calculated at the microphone position using Green's function. Whilst the measurement time was 10 s, the simulated time signal corresponds to a time of 0.075 s. A window length of 0.05 s and a sampling rate of 48 kHz were used for measured as well as simulated sound pressure spectra.

Although acoustic spectra are plotted up to 10 kHz, using SAS turbulence model is only appropriate for frequencies up to 3000 Hz. This was validated by measuring wall pressure fluctuations in the gap region. These were basic investigations which were carried out and are not illustrated in the scope of this paper.

For all investigated fan configurations measured and simulated, sound pressure levels show satisfying results in broadband noise from 200 up to 3500 Hz. In contrast to the measurements, the simulation results show peaks at the blade passing frequency of 360 Hz. In addition, the subharmonic peaks are not well captured using the FWH approach.

The simulation results using the PCWE formulation are presented in comparison with measured data as well. Figure 13 displays the SPL on the axis 1 m upstream of the radiator for the three considered fans.

With respect to the order of magnitude the simulation is able to reproduce the measurements quite well for the frequency range 400 Hz $\leq f \leq$ 2000 Hz. The narrowband component at $f = 600$ Hz is met precisely in all considered fan configurations. The calculation of the peaks at 300 Hz can be found in relative good agreement. As can be seen from Figure 14 radiated sound pressure of the configuration BS is significantly higher compared to the other fans, which correlates to measurements.

Document downloaded by @DAEL, 2026-11-24 19:32:23 - personal use only

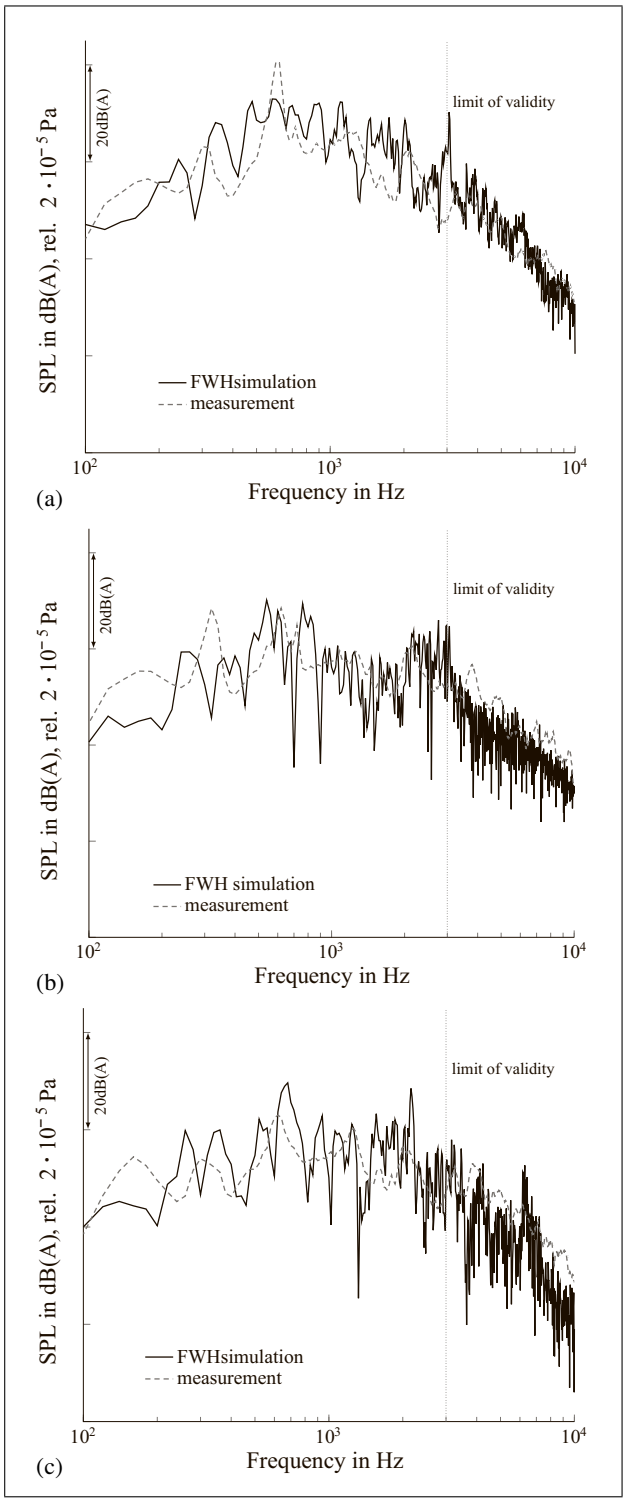


Figure 12. Comparison of measured and calculated FHW spectra of sound pressure level (SPL) at a microphone position 1 m coaxial upstream of the radiator. A stationary intigration surface is applied. (a) BS, (b) BM, (c) FS.

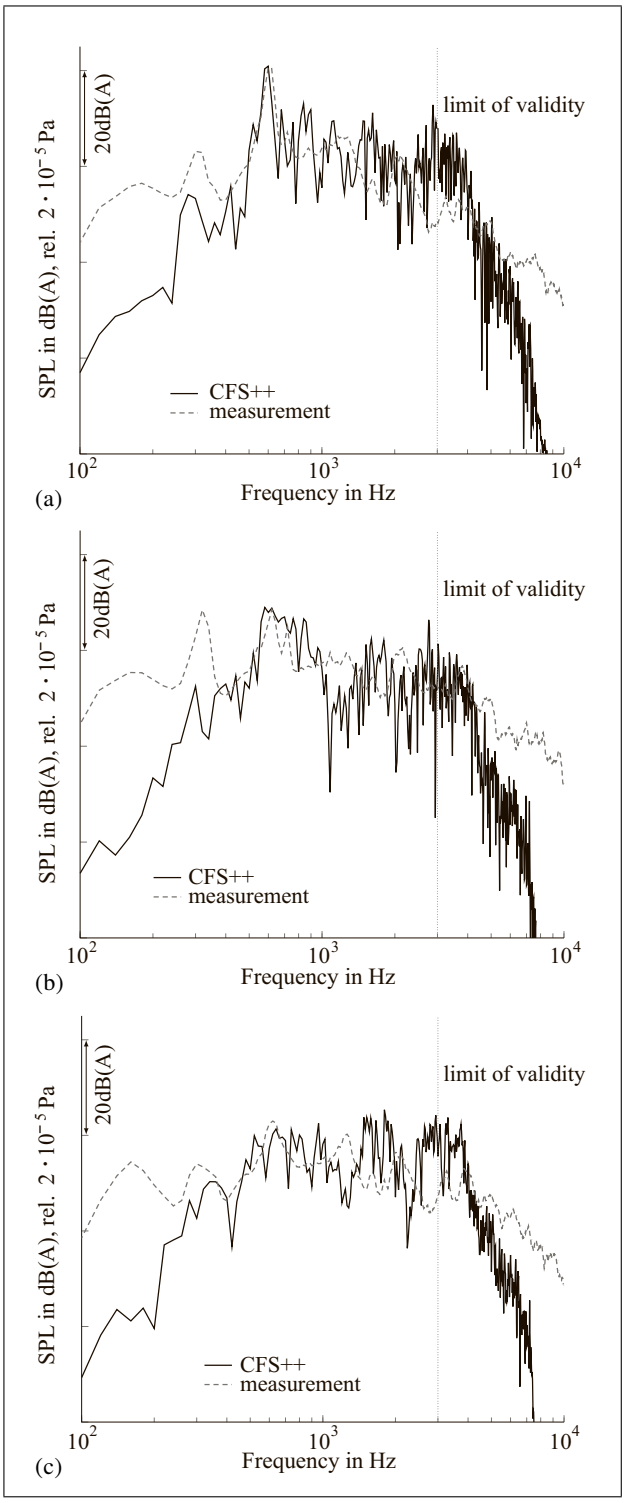


Figure 13. Spectra of sound pressure level (SPL) at a microphone position 1 m coaxial upstream of the radiator. Calculated using CFS++ and PCWE formulation. (a) BS, (b) BM, (c) FS.

The frequencies above 3000 Hz are propagated poorly by the grid spacing for the CFS++ acoustic simulation, which means the reference of 10 to 20 grid points per wavelength is not met. As a result the simulated spectra underestimate the radiated SPL.

6.2. Investigation of different levels of broadband noise and subharmonic peaks

To investigate the different sound pressure levels of broandband noise and subharmonic peaks, the integral method as well as the volume based method are used. As already shown in Section 6, the FWH approach is suitable

Document downloaded by @DAEL, 2026-11-24 19:32:23 - personal use only

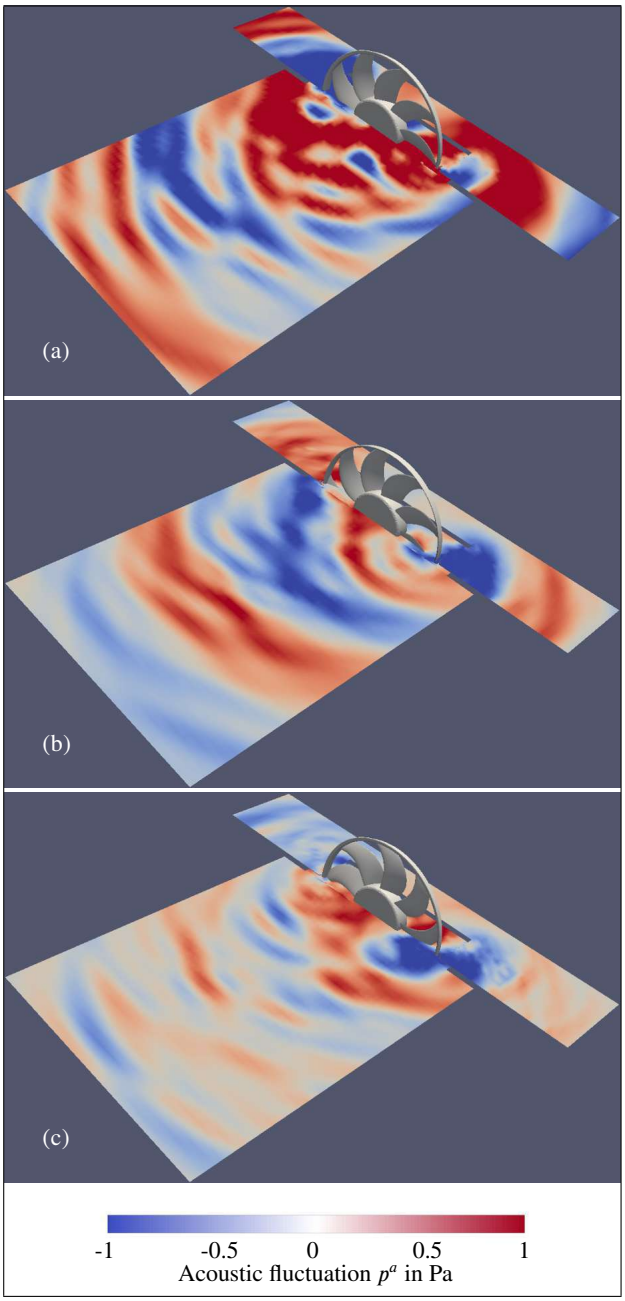


Figure 14. Propagation of acoustic pressure at time $t = 0.075$ s.

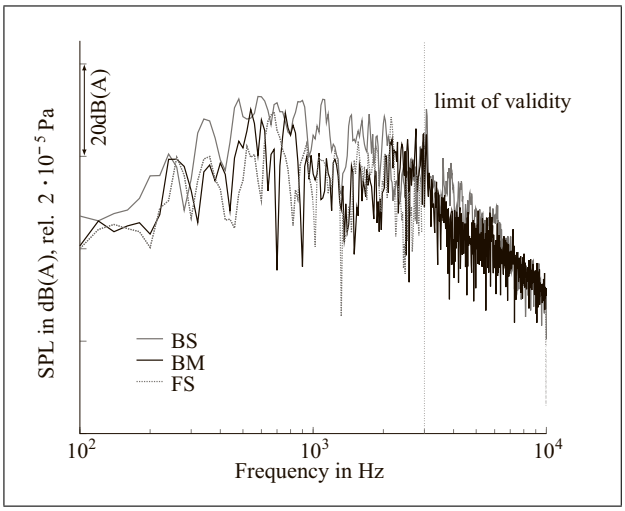


Figure 15. Calculated spectra of sound pressure level (SPL) at a microphone position 1 m coaxial upstream of the radiator. Here the FWH integration surface in stationary domain was utilized.

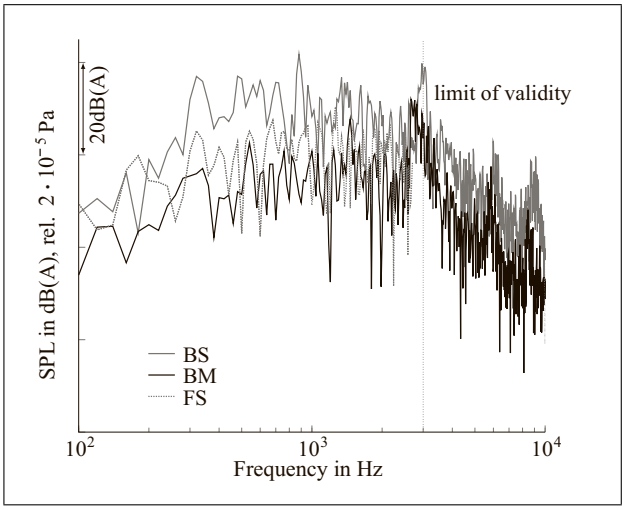


Figure 16. Calculated spectra of sound pressure level (SPL) at a microphone position 1 m coaxial upstream of the radiator. Here the FWH integration surface at the blade surface was utilized.

for the investigation of broadband differences in the low frequency range. Therefore, the source terms which are calculated on the integration surface located in the stationary domain as well as source terms which are calculated on a moving integration surface are used. By varying the integration surface it is possible to separate the acoustic sources.

Considering the presented SPL, it is obvious that the higher pressure fluctuations on the surfaces in the tip region are responsible for the higher sound production in the BS case. Since the integral approach is limited, the volume-based approach is applied to investigate the accentuated radiation due to higher pressure fluctuations on the surfaces in the tip region in more detail. Apart from propagation results as the main output of volume-based simulations the visualization of the acoustic sources lead to a better understanding of source mechanisms in the investigated geometry. For the calculation of the acoustic source terms, the right hand side of the PCWE (8) is applied. The advantage of this formulation compared to the Lighthill tensor is the possibility to calculate acoustic sources in the near field of the fan due to the seperation of hydrodynamic and acoustic pressure fluctuations. Figure 17 illustrates iso-surfaces of the acoustic sources at a time $t = 0.075$ s. The different colours indicate the phase shift of the occurring sources.

One can see that the PCWE formulation is able to produce sources that are very similar to those described in [1, 3, 4]. In addition to the sound production at leading and trailing edge, acoustic sources produced at the blade tips are dominant. In contrast to leading edge noise, trailing edge noise varies depending on blade skew. In the wake

Document downloaded by @DAEL, 2026-11-24 19:32:23 - personal use only

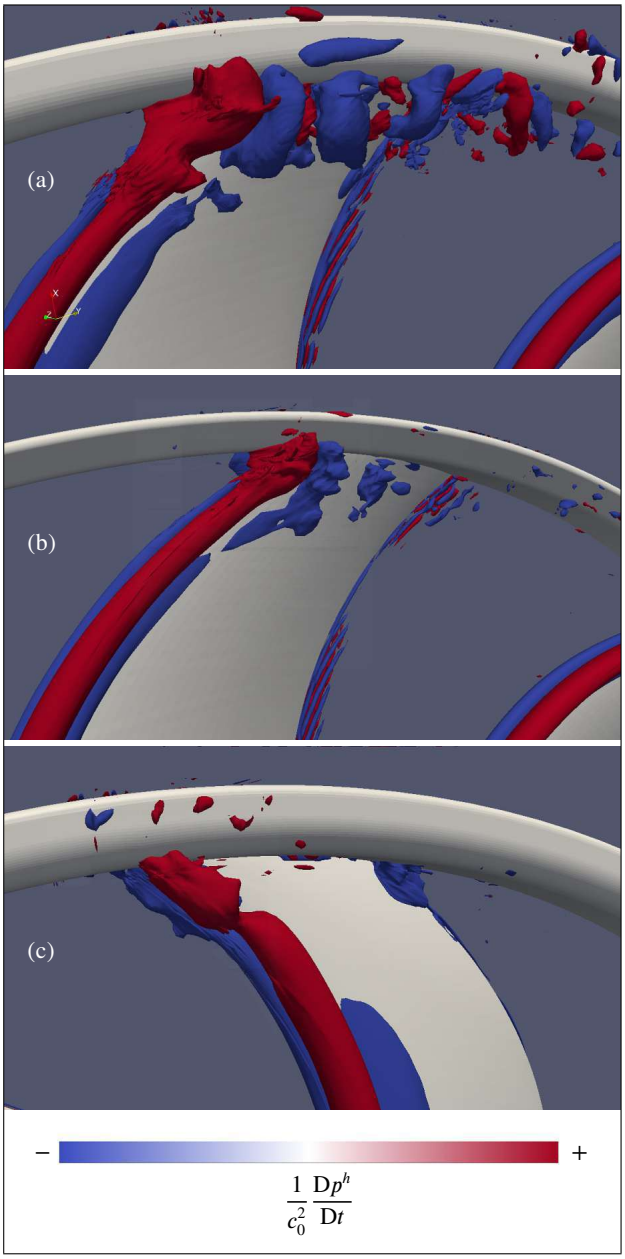


Figure 17. Iso-surfaces of PCWE acoustic sources around blade tip. View from suction side of the fan.

of the trailing edge of the backward skewed fans BS and BM, sources are produced due to the longer effective chord length and the highly developed boundary layer. The simulation of the forward skewed fan shows a lower source strength for trailing edge noise.

As expected, intensive source structures can be observed around the leading edge for all three fans. By studying those structures over different time steps one notices that they are stationary in the rotating system and move with the impeller speed. This distribution is due to interaction of the fan blades with the inflow and leading edge noise is the consequence [3].

The intensive sources, which occur at the blade tips just below the ring, are produced by the gap flow and the backflow beneath the ring. These sources differ in the underlying mechanism. A random distribution of sources at the blade tip that is generated by the recirculation area can be detected, especially in case of the configuration BS. Showing stochastic time behaviour, these sources radiate mostly broadband noise [3, 4]. In the case of BM, a reduction of the given source region is noticeable. An explanation for this development is the reduced interaction of the turbulent structures and the blade surfaces. To emphasize this broadband characteristic, frequency filtered PCWE source terms are illustrated in Figures 18 through 20. Therein surfaces are highlighted by source amplitude. The surface region of high source strength correlates to the the maximum surface pressure fluctuations, as observed in Figure 11.

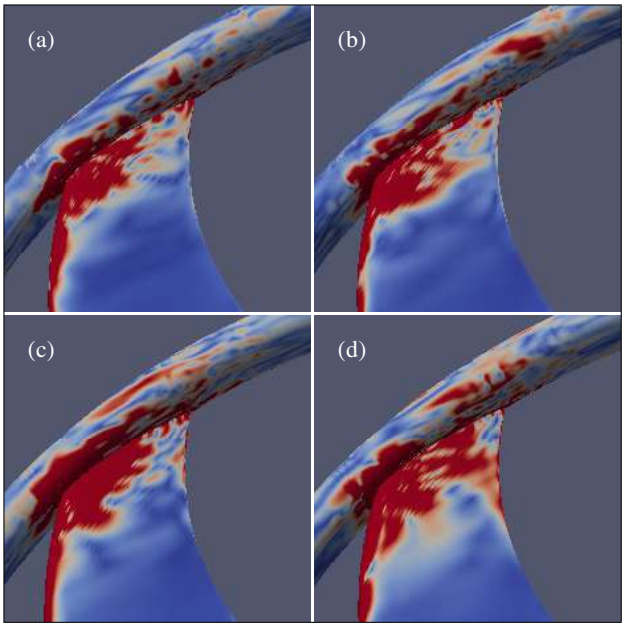


Figure 18. FFT filtered PCWE source terms on blade surface for the BS configuration. (a) 300 Hz, (b) 400 Hz, (c) 500 Hz, (d) 600 Hz.

Two large counterphase volume sources occur in Figure 17 which can be observed for all three fan configurations. These are due to coherent structures impinging on the blade tip as discussed in Figures 8 and 10. Given source terms exhibit a periodic pulsation while moving with the leading edge which suggests a tonal characteristic. Small source elements of these structures detach and travel along the blade tip showing a pulsating amplitude while dissipating. When comparing BS and FS configurations, the addressed source distribution is present in both cases but with differing intensity. Intensity being attenuated in the latter case. The modified gap also shows a slight reduction regarding this source distribution with respect to the standard gap.

The coherent structures produce acoustic sources while convecting towards the leading edge. This behaviour is illustrated in Figures 21 through 23. These sources interact with the blade surface and produce tonal and broadband noise. In contrast to the sources at 400 and 500 Hz sources appear regularly in case of 300 and 600 Hz. It is concluded that, given the periodic nature, the sources at

Document downloaded by @DAEL, 2026-11-24 19:32:23 - personal use only

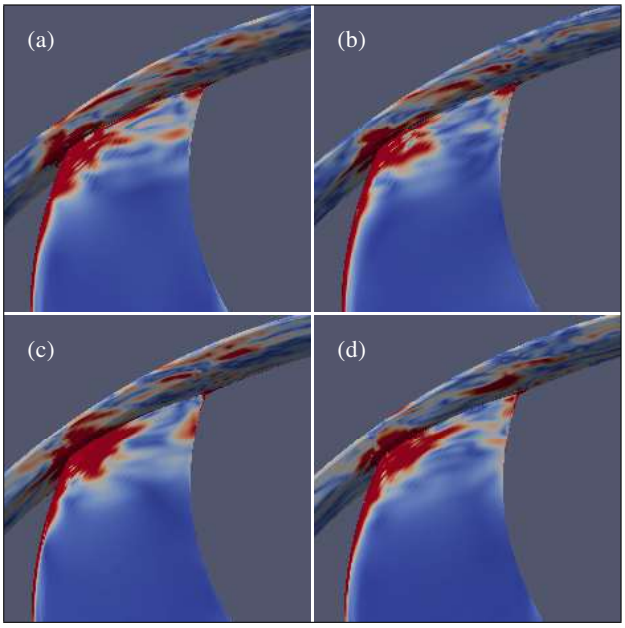


Figure 19. FFT filtered PCWE source terms on blade surface for the BM configuration. (a) 300 Hz, (b) 400 Hz, (c) 500 Hz, (d) 600 Hz.

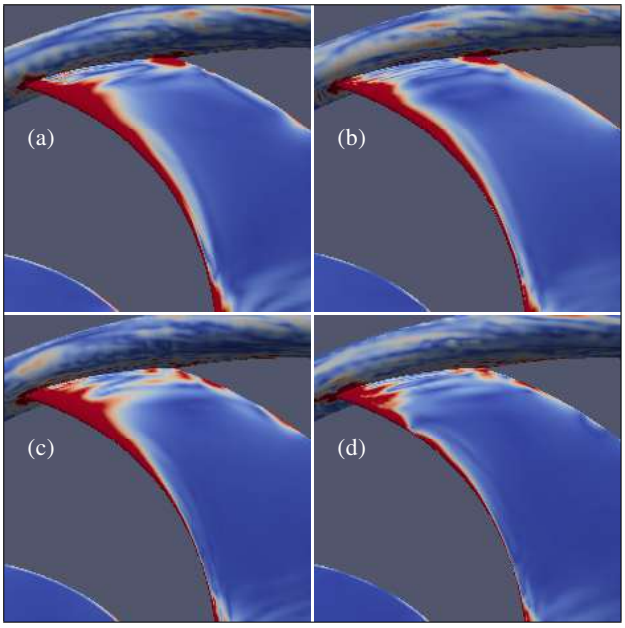


Figure 20. FFT filtered PCWE source terms on blade surface for the FS configuration. (a) 300 Hz, (b) 400 Hz, (c) 500 Hz, (d) 600 Hz.

300 and 600 Hz are due to the pulsating volume sources, referred to earlier. Therefore the narrowband subharmonic peaks are the outcome of the interaction of coherent structures of the gap flow with the leading edge. These coherent structures, that occur regularly as can be shown by the corresponding sources in Figures 21 through 23, radiate sound themselves. However, when interacting with the leading edge, pulsating volume sources are produced.

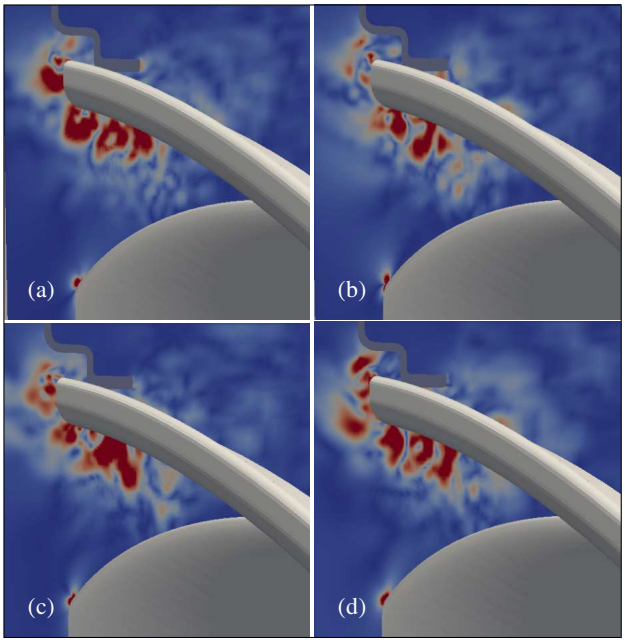


Figure 21. FFT filtered PCWE source terms on sectional view for the FS configuration. (a) 300 Hz, (b) 400 Hz, (c) 500 Hz, (d) 600 Hz.

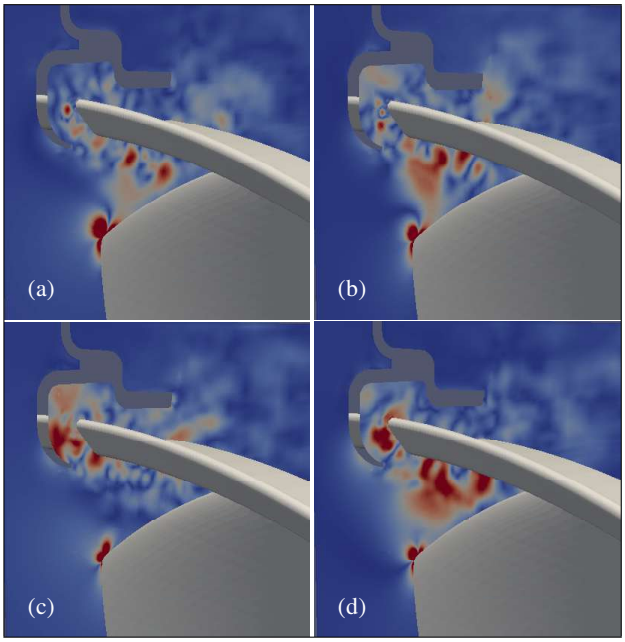


Figure 22. FFT filtered PCWE source terms on sectional view for the FS configuration. (a) 300 Hz, (b) 400 Hz, (c) 500 Hz, (d) 600 Hz.

7. Conclusions

The influence of fan blade skew and gap geometry on the flow field, the corresponding source mechanisms and sound propagation was investigated for three fan configurations. A backward skewed fan with a standard gap geometry, the same fan with a modified gap geometry and a forward skewed fan with the standard gap geometry were taken into account.

Document downloaded by @DAEL, 2026-11-24 19:32:23 - personal use only

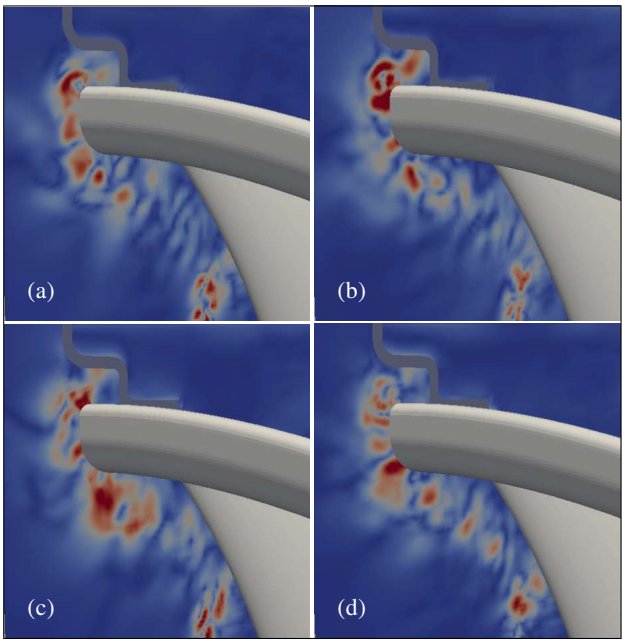


Figure 23. FFT filtered PCWE source terms on sectional view for the FS configuration. (a) 300 Hz, (b) 400 Hz, (c) 500 Hz, (d) 600 Hz.

Regarding flow simulation a SAS turbulence model was utilized. For acoustic simulations a FWH code and a volume-based method were applied.

The fluid mechanical results show different gap flow conditions at the suction side of the fan depending on gap and blade geometry. This leads to a production of turbulent structures interacting with the blade tips. For the BS configuration a spatially extended recirculation area needs to be emphasized. This recirculation area interacts with the fan blades and leads to the radiation of broadband noise. This was established utilizing the frequency filtered PCWE sources. Using FWH method, the calculation of this radiated broadband characteristic could be achieved in good agreement with measured data. It was shown that it is possible to reduce the radiation of broadband noise with the configurations BM and FS . The simulation using FWH method was able to reproduce this reduction in comparison to the measurements. Furthermore, it was demonstrated that the reduction in broadband noise is due to the decreased recirculation area and the inhibited interaction of the circulating flow with the blade surface. Analysing transient behaviour of the source terms as well as frequency filtered sources, this can be seen from the diminished extent of the random source pattern along the chord length for BM and FS configurations. The underlying effect supporting the reduced interaction of recirculation eddies and fan blades is their convection by the gap flow in case of BM . In case of the configuration FS a similar effect is achieved due to the different pressure distribution on the blade surface which reduces the deflection of the gap flow towards the hub. As the industrial development is concerned the objective must be, to find a fan blade geometry which influences the recirculation area advantageously. The main influencing factor is the blade skewness, which needs to be defined considering the existing inflow conditions.

In addition to broadband noise, tonal components can be observed in measured as well as simulated sound pressure spectra. In case of the BS dominant components at 300 and 600 Hz are present. For the other configurations these peaks are reduced which is also reproduced by the simulations. The subharmonic peaks are the outcome of coherent turbulent structures impinging on the leading edge. These structures originate in the gap flow and interact periodically with the blade tip. The source mechanism correlating to these subharmonic peaks is located at the leading edge just beneath the ring. For radiating tonal noise, these source structures exhibit a periodical pulsating behaviour while moving with the rotating system. In real cooling fan applications subharmonic peaks do not occur so prominently because the inflow conditions to the impeller are not as homogeneous. In contrast to this, source mechanisms radiating tonal noise at the BPF becomes intensified.

References

[1] T. Carolus: Ventilatoren. aerodynamischer entwurf, schallvorhersage, konstruktion. Springer, Wiesbaden, 2013, (3. Auflage).

[2] W. Neise: Lärm und lärmbekampfung bei ventilatoren - eine bestandsaufnahme. 1980.

[3] M. Zayani: Aeroakustisches betriebsverhalten von kfz-kühlerventilatoren. Dissertation Karlsruher Institut für Technologie (KIT), 2013.

[4] T. Wright: The Acoustic Spectrum of Axial Flow Machines. Journal of Sound and Vibration **45** (1976) 165–223.

[5] S. Magne, S. Moreau, A. Berry: Subharmonic tonal noise from backflow vortices radiated by a low-speed ring fan in uniform inlet flow. Journal of the Acoustical Society of America **137** (2015) 228–237.

[6] S. Moreau, M. Sanjose: Sub-harmonic broadband humps and tip noise in low-speed ring fans. Journal of the Acoustical Society of America **139** (2016) 118–127.

[7] J. Ffowcs Williams, D. Hawkings: Sound Generation by Turbulence and Surfaces in Arbitrary Motion. Philosophical Transactions of the Royal Society of London A: Mathematical, Physical and Engineering Sciences **264** (1969) 321–342.

[8] A. HÃijppe, J. Grabinger, M. Kaltenbacher, A. Reppenhagen, G. Dutzler, W. KÃijhnel: A non-conforming finite element method for computational aeroacoustics in rotating systems. American Institute of Aeronautics and Astronautics, Juni 2014.

[9] M. Kaltenbacher, A. Hüppe, A. Reppenhagen, F. Zenger, S. Becker: Computational aeroacoustics for rotating systems with application to an axial fan. AIAA Journal **55** (Nov. 2017) 3831–3838.

[10] R. Ewert, W. Schröder: Acoustic perturbation equations based on flow decomposition via source filtering. Journal of Computational Physics **188** (2003) 365–398.

[11] M. Kaltenbacher: Advanced simulation tool for the design of sensors and actuators. Procedia Engineering **5** (2010) 597–600.

[12] T. Heinemann: Axial fans under the influence of various uniform ambient flow fields. Dissertation. Friedrich-Alexander-Universität Erlangen-Nürnberg (FAU), 2018.

Document downloaded by @DAEL, 2026-11-24 19:32:23 - personal use only

[13] D. Casalino: An advanced time approach for acoustic analogy predictions. Journal of Sound and Vibration **261** (2003) 583– 612.

[14] M. Lighthill: On Sound Generated Aerodynamically. I. General Theory. Proceedings of the Royal Society of London A: Mathematical, Physical and Engineering Sciences **211** (1952) 564–587.

[15] M. Lighthill: On Sound Generated Aerodynamically. II. Turbulence as a Source of Sound. Proceedings of the Royal Society of London A: Mathematical, Physical and Engineering Sciences **222** (1954) 1–32.

[16] International Organization for Standardization. ISO 5801: 2007 Industrial Fans - Performance testing using standardized airways, 2007.

[17] F. Menter, Y. Egorov: A Scale-Adaptive Simulation Model using Two-Equation Models. AIAA 43. Aerospace Sciences Meeting and Exhibit; AIAA 2005-1095 (2005).

[18] J. Berenger: A perfectly matched layer for the absorption of electromagnetic waves. Journal of Computational Physics **114** (1994) 185–200.

[19] B. Kaltenbacher, M. Kaltenbacher, I. Sim: A modified and stable version of a perfectly matched layer technique for the 3-d second order wave equation in time domain with an application to aeroacoustics. Journal of Computational Physics **235** (2013) 407–422.

[20] I. Vaik, G. Paál, M. Kaltenbacher, S. Triebenbacher, S. Becker, I. Shevchenko: Aeroacoustics of the edge tone: 2D-3D coupling between CFD and CAA. Acta Acustica united with Acustica **99 no. 2** (2013) 245–259.

[21] M. Beiler: Untersuchung der dreidimensionalen strÃűmung durch axialventilatoren mit gekrÃijmmten schaufeln. VDI Verlag, DÃijsseldorf, 1996, (VDI-Fortschrittsberichte Nr. 298, Reihe 7: Strömungstechnik).

[22] F. J. Krömer: Sound emission of low-pressure axial fans under distorted inflow conditions. Dissertation. FAU University Press, 2018.

[23] T. Zhu, D. Lallier-Daniels, M. SanjosÃľ, S. Moreau, T. Carolus: Rotating coherent flow structures as a source for narrowband tip clearance noise from axial fans. Journal of Sound and Vibration **417** (2018) 198 – 215.

Document downloaded by @DAEL, 2026-11-24 19:32:23 - personal use only